Scaling dictates the decoder structure

Jingxiang Shen[1], Feng Liu[1,2], Chao Tang[1,2,3]*

[1]Center for Quantitative Biology, Peking University, Beijing 100871, China.

[2]School of Physics, Peking University, Beijing 100871, China.

[3]Peking-Tsinghua Center for Life Sciences, Peking University, Beijing 100871, China.

*Correspondence to: Chao Tang

Email: tangc@pku.edu.cn

Keywords: scaling, pattern formation, *Drosophila* gap gene, morphogen gradient, phenomenological decoder

Abstract

Despite variability in embryo size, the tissue, organ and body plan develop *in proportion* with embryo size, known as the scaling phenomenon. Scale-invariant patterning of gene expression is a common feature in development and regeneration, and can be generated by mechanisms such as scaling morphogen gradient and dynamic oscillation. However, whether and how static non-scaling morphogens (input) can induce a scaling gene expression (output) across the entire embryo is not clear. Here we show that scaling requirement sets severe constraints on the geometric structure of the input-output relation (the decoder), from which information about the regulation and mutants' behavior can be deduced without going into any molecular details. We demonstrate that the *Drosophila* gap gene system achieves scaling in the way that is entirely consistent with our theory. Remarkably, following the geometry dictated by scaling, a parameter-free decoder correctly and quantitatively accounts for the gap gene expression patterns in nearly all morphogen mutants. Furthermore, the regulation logic and the coding/decoding strategy of the gap gene system can also be revealed from the decoder geometry. Our work provides a general theoretical framework on a large class of problems where scaling output is induced by non-scaling input, as well as a unified understanding of scaling, mutants' behavior and regulation in the *Drosophila* gap gene and related systems.

Significance Statement

Within a given species, fluctuation in egg or embryo size is unavoidable. Despite this, the gene expression pattern and hence the embryonic structure often scale in proportion with the body length. This *scaling* phenomenon is very common in development and regeneration, and has long fascinated scientists. In this paper, the authors address the question of whether and how a scaling gene expression pattern can originate from non-scaling signals (morphogens). They found that scaling has profound implications in the developmental programming -- properties and behaviors of the underlying gene network can be deduced from the scaling requirement. They demonstrated that the scaling in fruit fly embryogenesis indeed works in this way. Thus, although biological regulatory systems are very complex in general, it can be forced to exhibit simple macroscopic behaviors due to selection pressure, as demonstrated in this study.

Main Text

Introduction

In development and regeneration, a cell has to know its position in space in order to determine its fate. Often this positional information is encoded in a space-dependent signal like morphogen gradient (1-3). The decoder in the cell (usually gene networks) reads the local value of the signal

to infer its spatial position by expressing the appropriate genes, as exemplified in the French-flag model (1, 4, 5).

A common feature in these processes is that the gene expression pattern generated by the decoder is often scale-invariant with respect to fluctuations in the overall length of the system, which ensures the organism develops in the correct proportion (6-11). A scale invariant output can be achieved with a scale invariant input. Indeed, this strategy is adopted by systems such as *Xenopus* embryo (12, 13), *Drosophila* wing (14-16) and probably *Drosophila* dorsoventral axis (17), where the morphogen itself manages to scale with the system size. Another mechanism known to generate a scaling pattern is dynamic oscillation, as seen in vertebrate somite segmentation (18-20), in which the oscillation period and the body axis elongation rate are tuned to adapt to altered embryo sizes. However, achieving scale-invariant patterning from non-scaling morphogens is still largely an open question. A prototypical example is the scaling of *Drosophila* segmentation gene patterning (8, 21-28), in which the gradients of the maternal morphogens seem to have fixed length constants, set by the diffusion constant and decay rate, that do not scale automatically with the embryo size (21, 26, 28-31). In this paper, we establish a general theoretical framework. We show that the necessary and sufficient condition for a decoder to generate a scale-invariant expression pattern from non-scaling morphogens contains rich information on the geometric structure of the decoder. We then provide strong evidences that *Drosophila* gap gene system achieves scaling in our proposed way. Our work provides a comprehensive understanding on this classic scaling problem.

Results

The Geometric Structure of the Decoder is Determined by the Scaling Requirement.

We first illustrate our basic idea using a bi-gradient kind toy model (1, 22, 32). In this simplified model, there are two morphogens, M_1 and M_2, having anterior and posterior exponential gradients with a fixed length constant λ (Fig. 1A, length of a standard-sized embryo is defined as L=1). For larger (smaller) embryos, the effective length constant should shrink (expand) if measured in the relative coordinate ($y \equiv x/L$, $M_1 = e^{-yL/\lambda}$, $M_2 = e^{-(1-y)L/\lambda}$, Fig. 1B). Consider for example the position y=0.35 as the boundary separating two different cell fates in the embryo. In a smaller (larger) embryo, as the absolute distance to both termini are shorter (longer) at this position, local levels of both morphogens are higher (lower). When L varies, the y=0.35 point traces out a line on the M_1-M_2 plane (Fig. 1C). Therefore, in order to achieve perfect scaling, this y-constant line must be followed by the decision boundary of the decoder, which maps a (M_1, M_2) pair to a gap gene expression state ("fate"). In other words, the requirement imposed by scaling is enough to determine the effective input-output relation (coloring scheme) of the decoder on the M_1-M_2 plane, no matter how the decoder is implemented biochemically. The cell fate can also be represented by its equivalent position in wild-type (WT), denoted as $\tilde{y}$. In this case:

$$\tilde{y}(M_1, M_2) = \frac{\ln M_1}{\ln M_1 M_2}\,. \tag{1}$$

Once determined by its scale-invariant performance in WT embryos, the same decoder can be applied to mutant embryos where the maternal morphogen profiles are perturbed but the decoding machines are intact. In the case considered here, all y points belonging to a WT embryo of size L correspond to the hyperbolic curve $M_1 \cdot M_2 = e^{-L/\lambda}$. On the other hand, consider a mutant embryo of which L=1 but the M_1 copy number is doubled:

$$M_1{}' = 2e^{-y_{mut}/\lambda},\ M_2{}' = e^{-(1-y_{mut})/\lambda}. \tag{2}$$

This mutant is also represented by a hyperbolic curve $M_1{}' \cdot M_2{}' = 2e^{-1/\lambda}$ (Fig. 1D). This curve is exactly the one corresponding to a WT embryo of size $L = 1 - \lambda \ln 2$, though points of the same cell fate locate at different y's in WT and the mutant. For example, the blue-green boundary at y=0.35 in WT is shifted to 0.46 in the mutant. In general, for any y_{mut} in this mutant embryo, there always exists a corresponding position y_{WT} in WT embryo with the same morphogen values, hence the same cell fate $\tilde{y}$:

$$y_{WT}(y_{mut}) \equiv \tilde{y}(y_{mut}) = \frac{y_{mut} - \lambda \ln 2}{1 - \lambda \ln 2}\,. \tag{3}$$

We call this mapping $\tilde{y}(y_{mut})$ the "fate-map" of this mutant, which can also be obtained by directly substituting Eq. 2 into Eq. 1. This fate map can be tested experimentally by plotting the positions y_{WT} against y_{mut} for the measured expression domain boundaries (Fig. 1E).

Construction of a Phenomenological Decoder for *Drosophila*.

Following the arguments represented in the last section, we next construct a decoder for the *Drosophila* gap gene system, using all the three maternal morphogen gradients Bcd, Nos/mHb and Tor. These three are also the only upstream-most gradients (33), since *bcd*$^-$*nos*$^-$*tor*$^-$ triple mutant shows spatially uniform gap gene expression (34, 35). Based on experimental data (26, 28, 36-40) and the minimal assumption that they all have fixed length constants, the profiles of the gradients are given by Eq. 4 below (see SI-1 and SI-6 for details) (Fig. 2A and Fig. S1).

$$\begin{cases} Bcd(y) = L^{\beta} e^{-yL/\lambda_B} \\ mHb(y) = mHb_0\left(1 + e^{\alpha L(y-1+(1-\lambda_H)/L)}\right)^{-1} \\ Tor(y) = e^{-yL/\lambda_T} + e^{-(1-y)L/\lambda_B} \end{cases} \tag{4}$$

The gap genes (*hb*, *Kr*, *kni* and *gt*) are the first set of zygotic segmentation genes downstream of the maternal morphogens, and the first to display a scaling pattern (21, 27). Therefore, by reading the non-scaling maternal morphogens, a robust and near-perfect scaling blueprint of future body plan is already established at the gap gene stage. This blueprint is believed to have enough information to uniquely determine the fate of each cell hereafter (41, 42).

The *Drosophila* embryo has around 100 rows of cells along the Anterior-Posterior (A-P) axis before gastrulation. Nearly any two of them can be distinguished by their gap gene expression (42), so there are effectively around 100 different cell fates along the A-P axis and the fate map $\tilde{y}$ should be discussed at the resolution of 0.01. To visualize these cell fates by colors, we group them into 8 classes according to the dominantly expressing gap gene (Fig. 2B). A standard-sized WT embryo is represented by a 1-d curve in the space of (Bcd, mHb, Tor). When L varies, this curve sweeps out a 2-d WT manifold. Following our arguments in Fig. 1, the ideal output of a scaling decoder on this WT manifold can be immediately determined – lines of constant y values should have the same cell fate (Fig. 2C).

In reality, *Drosophila melanogaster* embryo length varies approximately between 450 and 570 μm (~±10%) across different fly stocks (8). To have a more realistic picture, we hereafter sample L from a normal distribution $L \sim N(1,\ 0.1)$ to simulate the effects of length fluctuation across *Drosophila* stocks. Another important aspect is noise in morphogen profiles. When morphogen level approaches zero it should have huge relative noise thus cannot carry useful information. We introduced explicitly a Poisson noise term to the morphogen values to reflect this effect (See Methods and SI-2 for details). As a result, the "colored lines" in Fig. 2C now transform into the WT-point-cloud in Fig. 2D.

The gap gene network (i.e., the decoder) should be able to classify all the points in Fig. 2D into classes (real cell fate) that matches their colors. Besides just obtaining a classifier that performs the classification task (like a Bayesian one discussed in SI-5), we are more interested in figuring out the shape of those decision boundaries explicitly. Complexity and nonlinearity of the decision boundaries are directly related to whether it can be satisfactorily approximated by a gene regulation network as will be discussed later. Here comes an important observation, that for the *Drosophila* case the boundaries between regions of different colors are effectively linear – any decoder that achieves scaling by reading the local morphogen levels should effectively behave like a set of *linear* classifiers, at least within the WT point cloud. Therefore, we fit the phenomenological decision boundaries with planes (see Methods and SI-3 for details). Points of different colors seem to be separated satisfactorily in this way (Fig. 2, D and E, and Fig. S2D).

The three maternal gradients can not only determine boundaries of gap gene expression domains, but also ~100 distinct A-P cell fates as mentioned above. Thus, we can construct a (approximately) continuous version of the decoding function using more linear classifiers of this kind. Along the A-

P axis, we fit 100 such classification planes at 100 equally spaced y positions (see Methods and SI-3). The linear classifiers work sufficiently well with the decoding task, i.e., possible nonlinearities in the ideal classification boundaries can indeed be safely ignored. Fig. 2F shows the decoding result of the WT ensemble of Fig. 2D using the linear classifiers. Despite the presence of Poisson noise, positions ($\tilde{y}$) decoded by reading the maternal morphogen values are always close to the ground truth positions (y). The root-mean-square-error $RMSE = \sqrt{\langle(\tilde{y} - y)^2\rangle}$ is hardly larger than 1%, even smaller than the *RMSE* of a Bayesian decoder which allows arbitrary decision boundary geometry (SI-4 and Fig. S2).

The Decoder Quantitatively Predicts Phenotypes of Morphogen Mutants.

We next demonstrate that such a decoder, whose overall geometry is solely determined by scaling, has a remarkable power to predict nearly all phenotypes of morphogen mutants in *Drosophila*. Note that the values of (Bcd, mHb, Tor) in mutants may lie outside of the WT region (color point cloud in Fig. 2D). In this case, we linearly extrapolate the classification planes (see SI-4 for justification of the extrapolation).

Fig. 3A-C show the intersections of the linearly extrapolated classification planes with the bottom /left /back faces of the cube in Fig. 2D (marked by α /β /γ, on which Tor=0 /Bcd=0 /mHb=mHb_0), with the same color scheme as in Fig. 2. Maternal morphogen null mutants lie on these faces. For example, in the *nos*$^-$ mutant mHb is equal to mHb_0 throughout the entire embryo, corresponding to projecting the WT curve in the (Bcd, mHb, Tor) space onto the γ plane. It is clear in Fig. 3C that along this projected *nos*$^-$ curve, domain iv is followed immediately by domain vii, indicating the loss of abdominal *kni* (v) and *gt* (vi) domains. This is exactly the case observed in experiments (35, 43, 44). As another example, consider the *bcd*$^-$*tor*$^-$. mHb is now the only morphogen gradient, decreasing from its maximum value to zero from the anterior to posterior pole. It is obvious in Fig. 3A-B that points on the mHb axis fall into the iv, v and vi domains successively, corresponding to three gap gene domains *K*r, *kni* and *gt* appearing successively in this mutant embryo. As the Bcd=Tor=mHb=0 point is classified into domain vi, the *gt* domain should extend all the way to the posterior pole. This is also the pattern observed experimentally (34, 35).

More than the predictions on presence or absence of certain gap gene domains, a continuous valued fate map $\tilde{y}(y_{mut})$ can be constructed by incorporating all the 100 classification planes. In Fig. 3D, the predicted fate map for WT and 11 maternal morphogen mutants are shown as black curves. To test our predictions against experiments, we identify the peak and boundary positions for all gap gene domains (Table S1) from the published quantitative measurements of gap gene profiles in WT and various mutants (35, 45-47). For each of them, its position in mutant is plotted against its WT

positions (yellow squares in Fig. 3D). Remarkably, predictions and experiments are consistent in all cases.

Decoder Structure Reveals Features of Underlying Gene Regulation.

Predicted fate map can also be converted to a predicted gap gene pattern. For y_{mut} in a mutant embryo, the gap gene expression levels here can be approximated by the composite function $G\left(\tilde{y}(y_{mut})\right)$, where G stands for the WT gap gene pattern, and $\tilde{y}(y_{mut})$ is the fate map. Fig. 4A-B show two examples (solid lines). Measured profiles (35) are shown as dotted lines in lighter colors for comparison.

Further analysis reveals interesting connections between the decoder structure and the underlying gene regulation. Consider the *tor*$^-$ mutant as an example. As dictated by scaling, the decision boundaries *Kr-kni*, *kni-gt* and *gt-hb* should be inclined in 3-d, not perpendicular to the Bcd-mHb plane (Fig. 2E). This means that Tor should participate in positioning these boundaries to allow for scaling. Geometrically, when extrapolated to the Tor=0 plane following these inclined classification planes, a cell fate in WT should appear at a more posterior position than if being orthogonally projected downward. Thereby in the *tor*$^-$ mutant, besides that posterior *hb* domain disappears (48), the rest of the abdominal domains should also shift posteriorly. This prediction is fully consistent with experiments (Fig. 4A, where the filled and empty triangles mark the measured peak positions in *tor*$^-$ and WT, respectively).

This example may help us to understand the ubiquitous "redundant" regulations in the gap gene network. According to the simplest interpretation, mHb gradient defines the anterior boundary of abdominal *gt* (vi) domain through inhibition; Gt inhibits *kni*, thereby setting the posterior boundary of *kni* (v) domain (34). There is no "need", in principle, for Tor to be involved. But the observed shift of *kni* boundary in *tor*$^-$ clearly shows that in reality Tor contributes (probably through *tll*) to the repression on *kni* (44, 49, 50), setting its posterior boundary together with mHb as well as Bcd (51). We propose that such seemingly redundant regulations actually tune the slope of *kni-gt* classification plane, so that it could align with the angle required by scaling (Fig. 4C). Scaling seems to be one important "goal" of such redundancy in the gap gene network.

Another example deals with the *bcd*$^-$ mutant (Fig. 4B). Bcd is well known to function in the anterior part. However, the region where Bcd plays a role seems to be much wider than naively expected – *bcd*$^-$ mutant affects even domain vi and vii near the posterior pole. This aspect of Bcd should also contribute to tuning the decision boundary orientations to allow for scaling, as it has clearly been captured by our scaling-based phenomenological model. To be more precise, the decision plane representing the *gt-hb* (vi-vii) boundary at $\tilde{y}$=0.75 is:

$$-0.85Bcd - 0.12mHb + 0.45Tor = Const.,$$

indicating that Tor should be effectively an activator for *hb* here while Bcd should play a repressive role (Fig. 4D). This speculation is consistent with existing biological knowledges. Tor is long known to activate the posterior *hb* domain through *tailless* (*tll*) (49). And the effective repression by Bcd is most probably meditated by *Kr* and *kni*, upon whose mutation the posterior *hb* domain expands anteriorly (52).

A third example of this kind regards the head gap gene *orthodenticle* (*otd*), which is expressed between $\tilde{y}$=0.08 and 0.25 along the A-P axis. Position of the *otd* domain in mutants can be predicted straightforwardly by finding $\tilde{y}$=0.08 and 0.25 points in the corresponding mutant fate maps (Fig. 4E). These predictions are again in nice agreements with experiments (53): decreasing Bcd dosage shift both anterior and posterior *otd* boundaries anteriorly, while lacking Tor will make the *otd* domain fail to retract from the anterior pole, and shift its posterior boundary slightly forward. These observations in mutants are directly related to underlying regulations (as in (54)), that Bcd and Tor both activate *otd* in defining its posterior boundary, while at the same time both represses *otd* (most probably through *huckebein*) in setting the anterior boundary (Fig. 4F). The gap gene regulation network seems to be organized in such a way to allow scaling.

Different Morphogens Play Different Roles in Scaling.

In our framework, scaling originates from the insensitivity of decoder output to the correlated fluctuations in the local morphogen levels. The forms of such correlated fluctuations are determined by the morphogen profiles. Therefore, if the morphogen profiles were perturbed, the alignment between *y*-constant lines and the decoder's decision boundaries will be affected thus scaling would be as least partially destroyed. To provide quantitative tests of our model from this perspective, fate maps in mutant embryos with non-standard length ($L \neq 1.0$) are studied.

Missing Bcd destroys scaling completely and the gap gene pattern changes greatly with *L*. With decreasing embryo length, the *bcd*$^-$ embryo losses domains iv (*Kr*) and then v (*kni*) (Fig. 5A). A recent experiment (28) provides an excellent support for this prediction. (See Fig. S5C for detailed discussion). Increasing Bcd dosage also affects matching between the decoder and the *y*-constant lines. The mid-embryo *hb* boundary is reported to be unscaled in shortened embryos when Bcd dosage is doubled (28) (Fig. 5B, red dots), which is accurately capture by the decoder (Fig. 5B, black line. See also SI-8 for an analytical calculation).

In contrast to Bcd, missing mHb or Tor should have limited influence on scaling and affects only part of the embryo (Fig. 5C-D). The relative contributions to patterning and scaling from the three morphogens across the embryo can be quantitatively defined (SI-9) and are shown in Fig. 5E. Note

that the morphogen mHb has long been considered dispensable or redundant, since losing mHb does not lead to any direct loss of the segment (36, 37). However, our results indicate that it actually plays a crucial role for scaling in the abdominal region.

As a final example, we study the shift of cephalic furrow (CF) under mutation of the posterior or terminal morphogens plus Bcd dosage change. CF is the morphological boundary between head and thorax locating at y=0.344 in WT. It is a morphological trait much down-stream of the gap genes. But, as we believe that the scaling blueprint is established at the gap gene stage and passed down, we can regard CF as a hypothetical gap gene boundary $\tilde{y} = 0.344$ and predict its position $y \equiv X_{\mathrm{CF}}$ in various mutants. These predictions are compared with the measurements reported in (40) (Fig. 5, F-H).

When Bcd dosage is perturbed, the predicted X_{CF} matches well with experimental measurements (Fig. 5F). Note that X_{CF} shows robustness against Bcd dosage change – its shift is always visibly *smaller* than that of the iso-concentration point of Bcd (Fig. 5, gray dashed line).

Truly nontrivial are the cases when Bcd dosage is altered in the absence of mHb or Tor gradient. For example, in *nos*$^-$ mutant where mHb gradient is eliminated (Fig. 5G), with *increasing* Bcd dosage such robustness disappears, and X_{CF} follows the Bcd threshold exactly (marked by white arrow); while for *decreasing* Bcd dosage, such robustness still exists (black arrow). Similar but opposite phenomenon is seen in *tor*$^-$ mutant (Fig. 5H). These phenomena are successfully captured by our model without any further tuning on parameters. Shift of CF in these cases can be easily understood from information provided in Fig. 5E – Bcd and Tor are the main contributing bi-gradient pair anterior to the CF, while the Bcd-mHb pair dominants the middle part behind CF. Therefore, positional robustness of the CF upon Bcd dosage change has different origins when shifted anteriorly or posteriorly.

The Scaling Decoder Can be Implemented with Gene Regulation.

The discussions so far are quite general, independent of the detailed biochemical implementations of the decoder. In this section we provide evidence that the scaling decoder can be implemented by gene regulation and more specifically by the known gap gene network.

First, consider a toy model with a static anterior morphogen B (like Bcd) of fixed length constant and a single gap gene H whose initial condition H_{init} serves as the second posterior gradient (like mHb) (Fig. 6A). The desired output is to have H being activated in the anterior half with the boundary locating at y=0.5 regardless of the embryo length L. This requires that morphogen levels marked by the black dots or empty triangles (Fig. 6A) should both lie on the H boundary. The regulation network follows that of the inset in Fig. 6B. From a dynamical perspective, this network

is well known to have bi-stability and Fig. 6B shows a typical bifurcation diagram. Within the bistable range, the *H-high/H-low* states are separated by a critical line (red squares), which means exactly the decision boundary between cell fates. If the activation strengths are properly tuned, this critical line can be adjusted to have identical slope as the desired decision boundary in Fig. 6C. Such first-order approximation is already good enough for $\pm 20\%$ variations in embryo length.

The gap gene network has more degrees of freedom and more scaling boundaries, and does not necessarily have to reach a dynamical attracting point. But the general idea is the same. Based on the known gap gene network shown in Fig. 6D (33), we construct a differential equation model (see SI-11 for details). If fitted to the WT data (46) plus scaling requirement, the model can produce very similar decision boundaries as the phenomenological decoder (Fig. 6, E and F), hence correct predictions on mutants.

Discussion

Scale-invariant gene patterning can originate from integrative decoding of non-scaling signals. In this case, the effective input-output structure of the decoder is largely dictated by the requirement of scaling. Consequently, the underlying gene regulation system evolves to have its macroscopic behavior approximating the ideal decoder geometry. All the intricate biochemical details seem to be hidden and largely irrelevant.

We provided strong evidences that scaling in the *Drosophila* gap gene expression patterns indeed emerge in this way. There are quantitative agreements between model predictions and experiments on nearly all maternal morphogen mutants. We then showed that the scaling requirement alone contains rich information about the overall gene regulation logic and the way the morphogen signals are being integrated. The decoder was further demonstrated to be implementable by dynamical gene regulation models, and consistent with the existing knowledge of the gap gene regulation network.

Overall, our results provide a unified understanding to scaling, mutants' behavior and gene regulation in the *Drosophila* gap gene system. Since our framework is rather general, the arguments presented in this paper can be readily extended to other systems where scaling is achieved through integrating non-scaling morphogens. In SI-13, we discuss such an example: the long-germband insect *Megaselia abdita*.

Methods

Fitting the linear classification planes.

The WT point cloud (Fig. 2d) used for fitting the linear classification planes are generated as follows. First, the A-P axis is discretized into 101 points y=0% to 100%. For each of the y position, we sample 400 embryo length values from the normal distribution L~N(1, 0.1) and calculate the corresponding (Bcd, mHb, Tor) levels using equation (4). The three morphogen values are noted by $\boldsymbol{m}=(m_1, m_2, m_3)$ for convenience. Obviously, $0<m_{1,3}<1$ and $0<m_2<\mathrm{mHb}_0$ (mHb_0=0.1 here).

Then, a Poisson noise is added to each m_i by assuming the actual number of molecules is a Poisson variable n_i with $\langle n_i\rangle=N*m_i$, and the final morphogen value with noise is n_i/N. The maximum molecule number N controls the noise magnitude, and set to N=1000 throughout the main text. Note that we do not claim that the *actual* morphogen noise follows independently identically Poisson distribution. And N does *not* correspond directly to the number of molecules per nucleus. Instead, N=1000 is chosen to make the positional error of Bcd gradient close to that measured by Gregor, et. al.(55) (about 1~2% embryo length in the anterior half of embryo). Our model is not sensitive to the exact value of N, see Extended Data Fig. 4, g-h for the results for N=500 or 2000.

The entire point cloud in Fig. 2d thus consists of 101 subsets $\boldsymbol{m}|_y$, each of them have 400 points. The 100 classification planes are located at y=0.5%, 1.5%, …, 99.5%, denoted as classifiers #1, …, #100. Since gap gene expression is affected by the dorsoventral system when being very close to embryo termini, only classifiers #6 to #95 are considered in the main text. Each of the planes should perform the *local* classification task of distinguishing adjacent $\boldsymbol{m}$ point sets. For example, the plane locates at y=2.5% should go through the *noise-free* y=2.5% point for *standard-sized* embryo $\boldsymbol{m}|_{L=1,y=2.5\%}$ by itself. And its orientation is such that it can best distinguishing the point sets $\bigcup_L \bigcup_{y=\{0\%,1\%,2\%\}} \boldsymbol{m}|_y$ against $\bigcup_L \bigcup_{y=\{3\%,4\%,5\%\}} \boldsymbol{m}|_y$. To find the best plane orientation numerically, we simply enumerate the Euler angles θ and φ of its normal vector at the resolution of 1° and find the one with the highest classification accuracy.

The noise due to finite sampling and discretizing θ and φ can be eliminated by averaging the classification plane orientations for 25 repeats of the above sampling and fitting steps.

Predicting the fate-map function with the ensemble of linear classifiers.

In principle, 100 well-separated planes should divide the morphogen space (the cube with $0<m_1<1$, $0<m_2<0.1$, $0<m_3<1$) into 101 slices, corresponding to $\tilde{y}$=0% to 100%. If a query $\boldsymbol{m}$ point falls into the slice $\tilde{y}$=n%, it locates on the posterior side of classification planes #1 through #n, and on the anterior side of planes #n+1 to #100. Therefore, the corresponding cell fate $\tilde{y}$ can be read out from the classification results of all the linear classification planes (SI-2).

In some situations, however, the 100 linear classifiers could have contradictory outputs. Say, a point may be classified to the posterior side by classifier #70 but to the anterior side by #30. We

introduce a “posterior dominance rule” to tackle this difficulty. Anytime when this happens, output of the anterior classifier (#30 here) is always ignored. The reason for us to introduce the posterior dominance rule is simple – some anterior classification planes may intersect with the much more posterior region of the point cloud, vary far from where they were fitted (Fig. S3B). This posterior dominance rule works well, and finally yields all the results in Figs. 2-5.

Acknowledgments

We thank Timothy Saunders for providing data for Fig. S5 B&E.

References

1. L. Wolpert, Positional information and the spatial pattern of cellular differentiation. *J Theor Biol* **25**, 1-47 (1969).
2. D. St Johnston, C. Nusslein-Volhard, The origin of pattern and polarity in the Drosophila embryo. *Cell* **68**, 201-219 (1992).
3. J. B. Gurdon, P. Y. Bourillot, Morphogen gradient interpretation. *Nature* **413**, 797-803 (2001).
4. O. Crauk, N. Dostatni, Bicoid determines sharp and precise target gene expression in the Drosophila embryo. *Curr Biol* **15**, 1888-1898 (2005).
5. E. Bier, E. M. De Robertis, BMP gradients: A paradigm for morphogen-mediated developmental patterning. *Science* **348**, aaa5838 (2015).
6. J. Briscoe, S. Small, Morphogen rules: design principles of gradient-mediated embryo patterning. *Development* **142**, 3996-4009 (2015).
7. B. Z. Shilo, N. Barkai, Buffering Global Variability of Morphogen Gradients. *Dev Cell* **40**, 429-438 (2017).
8. S. E. Lott, M. Kreitman, A. Palsson, E. Alekseeva, M. Z. Ludwig, Canalization of segmentation and its evolution in Drosophila. *Proc Natl Acad Sci U S A* **104**, 10926-10931 (2007).
9. T. Bollenbach *et al.*, Precision of the Dpp gradient. *Development* **135**, 1137-1146 (2008).
10. M. Almuedo-Castillo *et al.*, Scale-invariant patterning by size-dependent inhibition of Nodal signalling. *Nat Cell Biol* **20**, 1032-1042 (2018).
11. D. Capek, P. Muller, Positional information and tissue scaling during development and regeneration. *Development* **146** (2019).
12. D. Ben-Zvi, B. Z. Shilo, A. Fainsod, N. Barkai, Scaling of the BMP activation gradient in Xenopus embryos. *Nature* **453**, 1205-1211 (2008).
13. D. Ben-Zvi, N. Barkai, Scaling of morphogen gradients by an expansion-repression integral feedback control. *Proc Natl Acad Sci U S A* **107**, 6924-6929 (2010).
14. S. Restrepo, K. Basler, Morphogen gradients: expand and repress. *Curr Biol* **21**, R815-817 (2011).
15. D. Ben-Zvi, G. Pyrowolakis, N. Barkai, B. Z. Shilo, Expansion-repression mechanism for scaling the Dpp activation gradient in Drosophila wing imaginal discs. *Curr Biol* **21**, 1391-1396 (2011).
16. F. Hamaratoglu, A. M. de Lachapelle, G. Pyrowolakis, S. Bergmann, M. Affolter, Dpp signaling activity requires Pentagone to scale with tissue size in the growing Drosophila wing imaginal disc. *PLoS Biol* **9**, e1001182 (2011).
17. N. Rahimi *et al.*, A WntD-Dependent Integral Feedback Loop Attenuates Variability in Drosophila Toll Signaling. *Dev Cell* **36**, 401-414 (2016).
18. J. Cooke, Control of somite number during morphogenesis of a vertebrate, Xenopus laevis. *Nature* **254**, 196-199 (1975).
19. V. M. Lauschke, C. D. Tsiairis, P. Francois, A. Aulehla, Scaling of embryonic patterning based on phase-gradient encoding. *Nature* **493**, 101-105 (2013).
20. O. Pourquié, The segmentation clock: Converting embryonic time into spatial pattern. *Science* **301**, 328-330 (2003).
21. B. Houchmandzadeh, E. Wieschaus, S. Leibler, Establishment of developmental precision and proportions in the early Drosophila embryo. *Nature* **415**, 798-802 (2002).

403 22. B. Houchmandzadeh, E. Wieschaus, S. Leibler, Precise domain specification in the
404 developing Drosophila embryo. *Phys Rev E Stat Nonlin Soft Matter Phys* **72**, 061920
405 (2005).
406 23. Manu *et al.*, Canalization of gene expression in the Drosophila blastoderm by gap gene
407 cross regulation. *PLoS Biol* **7**, e1000049 (2009).
408 24. S. Vakulenko, Manu, J. Reinitz, O. Radulescu, Size Regulation in the Segmentation of
409 Drosophila: Interacting Interfaces between Localized Domains of Gene Expression
410 Ensure Robust Spatial Patterning. *Phys Rev Lett* **103** (2009).
411 25. A. M. de Lachapelle, S. Bergmann, Precision and scaling in morphogen gradient read-
412 out. *Mol Syst Biol* **6**, 351 (2010).
413 26. D. Cheung, C. Miles, M. Kreitman, J. Ma, Scaling of the Bicoid morphogen gradient by a
414 volume-dependent production rate. *Development* **138**, 2741-2749 (2011).
415 27. H. Wu, Manu, R. Jiao, J. Ma, Temporal and spatial dynamics of scaling-specific features
416 of a gene regulatory network in Drosophila. *Nat Commun* **6**, 10031 (2015).
417 28. A. Huang, J. F. Rupprecht, T. E. Saunders, Embryonic geometry underlies phenotypic
418 variation in decanalized conditions. *Elife* **9** (2020).
419 29. D. M. Holloway, L. G. Harrison, D. Kosman, C. E. Vanario-Alonso, A. V. Spirov, Analysis of
420 pattern precision shows that *Drosophila* segmentation develops substantial
421 independence from gradients of maternal gene products. *Dev Dynam* **235**, 2949-2960
422 (2006).
423 30. F. Sprenger, C. Nusslein-Volhard, Torso Receptor Activity Is Regulated by a Diffusible
424 Ligand Produced at the Extracellular Terminal Regions of the Drosophila Egg. *Cell* **71**,
425 987-1001 (1992).
426 31. M. Coppey, A. N. Boettiger, A. M. Berezhkovskii, S. Y. Shvartsman, Nuclear trapping
427 shapes the terminal gradient in the Drosophila embryo. *Curr Biol* **18**, 915-919 (2008).
428 32. P. McHale, W. J. Rappel, H. Levine, Embryonic pattern scaling achieved by oppositely
429 directed morphogen gradients. *Phys Biol* **3**, 107-120 (2006).
430 33. J. Jaeger, The gap gene network. *Cell Mol Life Sci* **68**, 243-274 (2011).
431 34. G. Struhl, P. Johnston, P. A. Lawrence, Control of Drosophila body pattern by the
432 hunchback morphogen gradient. *Cell* **69**, 237-249 (1992).
433 35. M. D. Petkova, G. Tkacik, W. Bialek, E. F. Wieschaus, T. Gregor, Optimal Decoding of
434 Cellular Identities in a Genetic Network. *Cell* **176**, 844-855 e815 (2019).
435 36. V. lrish, R. Lehmannt, M. Akam, The *Drosophila* posterior-group gene *nanos* functions by
436 repressing *hunchback* activity. *Nature* **338**, 646-648 (1989).
437 37. M. Hulskamp, C. Schroder, C. Pfeifle, H. Jackle, D. Tautz, Posterior segmentation of the
438 Drosophila embryo in the absence of a maternal posterior organizer gene. *Nature* **338**,
439 629-632 (1989).
440 38. G. Struhl, Differing strategies for organizing anterior and posterior body pattern in
441 Drosophila embryos. *Nature* **338**, 741-744 (1989).
442 39. E. Poustelnikova, A. Pisarev, M. Blagov, M. Samsonova, J. Reinitz, A database for
443 management of gene expression data in situ. *Bioinformatics* **20**, 2212-2221 (2004).
444 40. F. Liu, A. H. Morrison, T. Gregor, Dynamic interpretation of maternal inputs by the
445 Drosophila segmentation gene network. *Proc Natl Acad Sci U S A* **110**, 6724-6729 (2013).
446 41. R. Lehmann, H. G. Frohnhofer, Segmental Polarity and Identity in the Abdomen of
447 Drosophila Is Controlled by the Relative Position of Gap Gene-Expression. *Development*
448 **107**, 21-29 (1989).

42. J. O. Dubuis, G. Tkacik, E. F. Wieschaus, T. Gregor, W. Bialek, Positional information, in bits. *Proc Natl Acad Sci U S A* **110**, 16301-16308 (2013).
43. E. D. Eldon, V. Pirrotta, Interactions of the Drosophila gap gene *giant* with maternal and zygotic pattern-forming genes. *Development* **111**, 367-378 (1991).
44. M. Rothet, E. A. Wimmer, M. J. Pankratz, M. Gonzalez-Gaitan, H. Jackle, Identical transacting factor requirement for knirps and knirps-related gene expression in the anterior but not in the posterior region of the *Drosophila* embryo. *Mechanism of Development* **46**, 169-181 (1994).
45. E. A. Wimmer, S. M. Cohen, H. Jäckle, C. Desplan, *buttonhead* does not contribute to a combinatorial code proposed for *Drosophila* head development. *Development* **24**, 1509-1517 (1997).
46. J. O. Dubuis, R. Samanta, T. Gregor, Accurate measurements of dynamics and reproducibility in small genetic networks. *Mol Syst Biol* **9**, 639 (2013).
47. A. Ochoa-Espinosa, D. Yu, A. Tsirigos, P. Struffi, S. Small, Anterior-posterior positional information in the absence of a strong Bicoid gradient. *Proc Natl Acad Sci U S A* **106**, 3823-3828 (2009).
48. R. Kraut, M. Levine, Spatial regulation of the gap gene *giant* during Drosophila development. *Development* **111**, 601-609 (1991).
49. G. Bronner, H. Jackle, Control and function of terminal gap gene activity in the posterior pole region of the Drosophila embryo. *Mech Dev* **35**, 205-211 (1991).
50. M. J. Pankratz, M. Hoch, E. Seifert, H. Jackle, Kruppel requirement for knirps enhancement reflects overlapping gap gene activities in the Drosophila embryo. *Nature* **341**, 337-340 (1989).
51. R. Rivera-Pomar, X. Lu, N. Perrimon, H. Taubert, H. Jackle, Activation of posterior gap gene expression in the *Drosophila* blastoderm. *Nature* **376**, 253-256 (1995).
52. S. Surkova *et al.*, Quantitative dynamics and increased variability of segmentation gene expression in the *Drosophila Kruppel* and *knirps* mutants. *Dev Biol* **376**, 99-112 (2013).
53. R. Finkelstein, N. Perrimon, The Orthodenticle Gene Is Regulated by Bicoid and Torso and Specifies Drosophila Head Development. *Nature* **346**, 485-488 (1990).
54. Q. Gao, Y. Wang, R. Finkelstein, Orthodenticle regulation during embryonic head development in Drosophila. *Mech Dev* **56**, 3-15 (1996).
55. T. Gregor, D. W. Tank, E. F. Wieschaus, W. Bialek, Probing the limits to positional information. *Cell* **130**, 153-164 (2007).

Figures

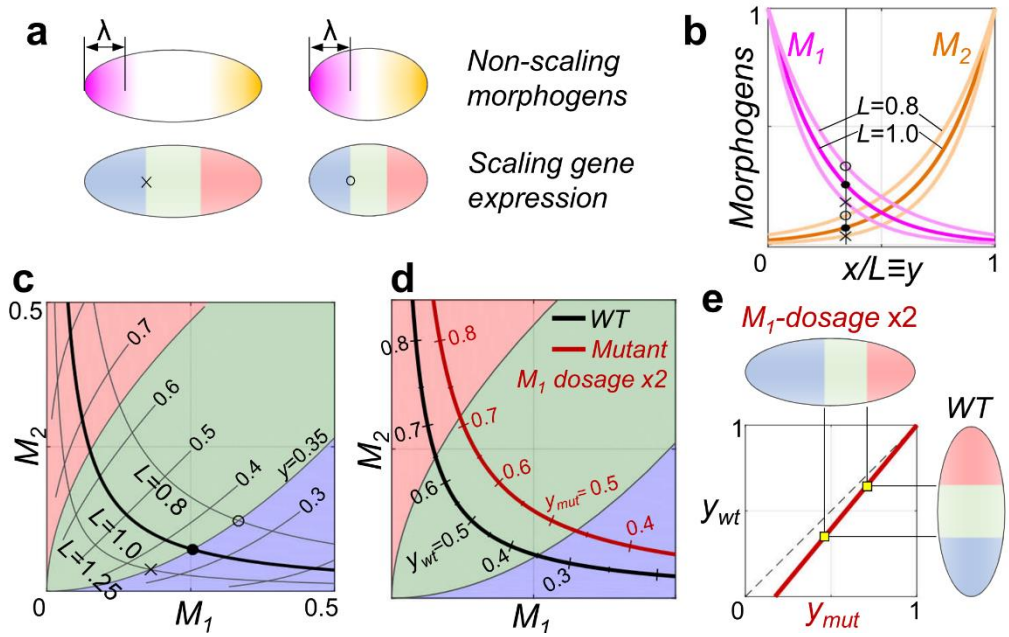

Figure 1. Generating scaling output by reading the local values of two non-scaling gradients.

(A) A schematic sketch with two embryos of different sizes. The two morphogen gradients are shown in the upper panel and the desired scaling output patterns are shown below.

(B) The same relative position $y \equiv x/L$=0.35 has higher level of both morphogens in a smaller embryo (marked by "o") than a larger one ("x").

(C) In the M_1-M_2 space, the standard-sized WT embryo is represented by the black curve. As L varies, the y=0.35 point traces out a line.

(D) Maternal morphogen profiles in a mutant are also represented by a curve in the M_1-M_2 space. The red curve stands for an L=1 embryo where the M_1 dosage is doubled. The corresponding cell fates along this red curve, hence along the A-P axis of this mutant, can be directly read out.

(E) The predicted "fate map" of the mutant in (C). All gene expression boundaries, if their positions in WT were plotted against their shifted positions in the mutant, should lie on the fate map.

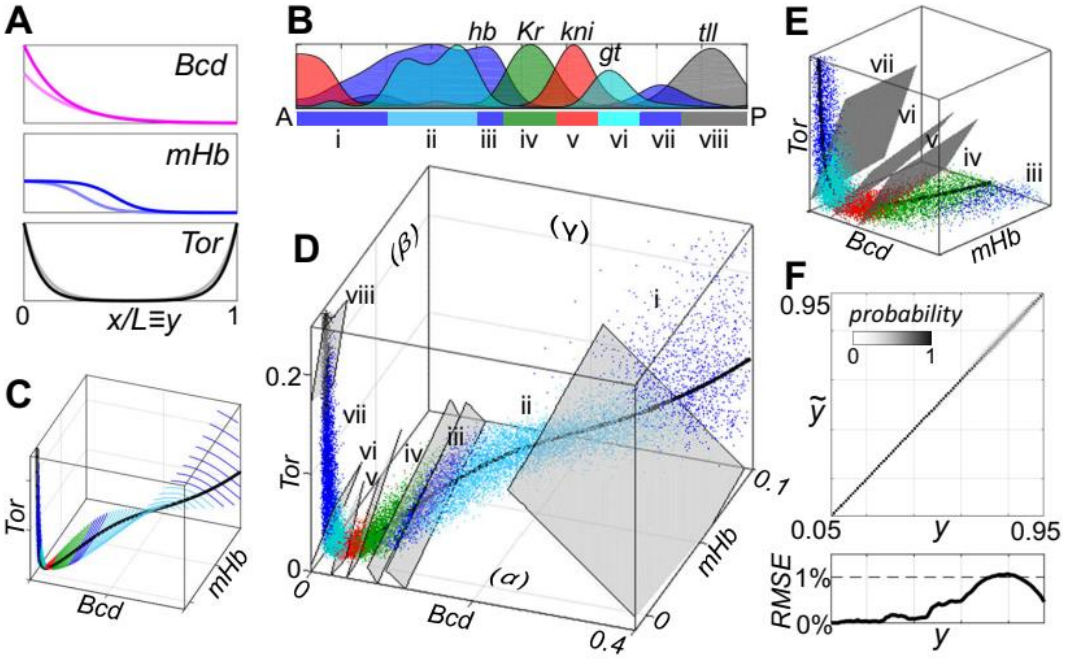

Figure 2. The structure of a phenomenological decoder of *Drosophila*.

(A) The three non-scaling maternal gradients in the coordinate normalized by embryo length $y \equiv x/L$ (Eq. 4). The morphogen profiles for a standard size WT embryo (L=1, darker lines) and a smaller one (L=0.8, lighter lines) are shown.

(B) About 100 different cell fates along the A-P axis are grouped into 8 domains according to the gap gene expression. The normalized gap gene profiles are adopted from (*36*) and a Gaussian smoothing is applied.

(C) In the (Bcd, mHb, Tor) space, the standard-sized WT embryo is represented by the black curve along which y varies from 0 to 1. When L changes, each point on this curve traces out a line representing the morphogen values at this y position in WT embryos of different sizes. Only the region corresponding to L=0.8~1.2 are plotted here. The y lines shown there have spacing 0.01 along the A-P axis.

(D) A Poisson noise is added to the morphogen levels and the embryo length is sampled from a normal distribution, turning the 2-d WT manifold in (C) to a point cloud. The decision boundaries can be well approximated by a set of linear planes.

(E) A magnification of (D). The iv-v, v-vi and vi-vii boundary planes are shown.

(F) Positions decoded from the morphogen values ($\tilde{y}$) *vs*. the ground truth (y) for the WT point cloud in (D). Since gap gene expression is affected by the Dorsal-Ventral system when being very close to embryo termini, we only discuss y between 0.05 and 0.95 hereafter. The root-mean-square-error is hardly larger than 1%

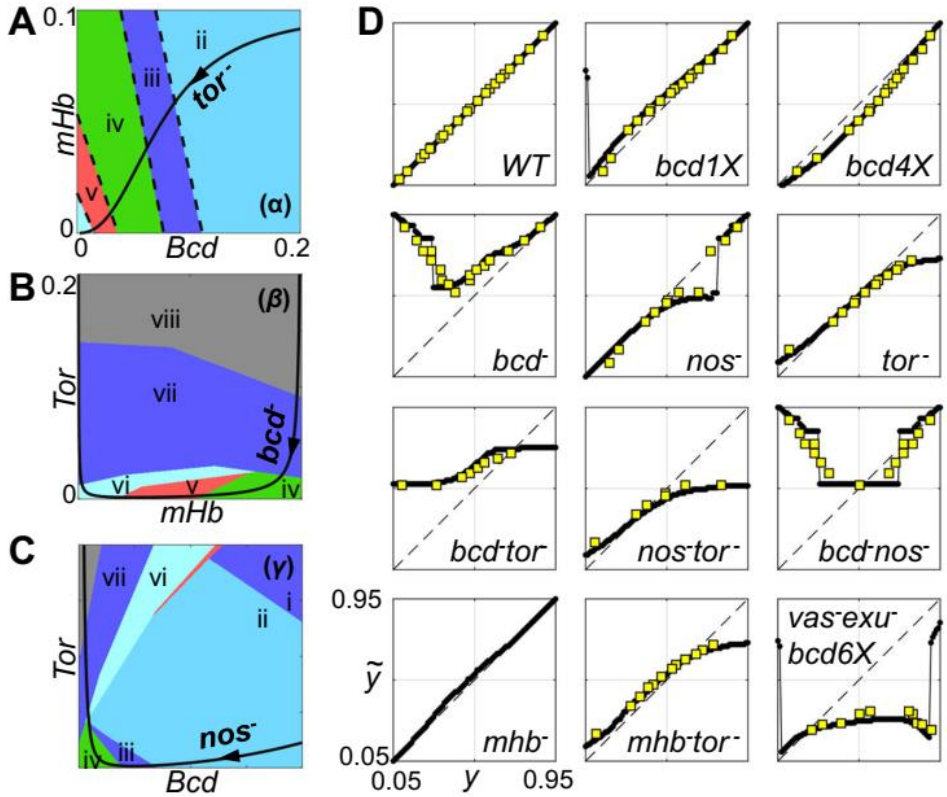

Figure 3. Quantitative predictions on mutant fate maps by the phenomenological decoder.

(A-C) The decoding results on the bottom/left/back faces (marked by α/β/γ) of the cube in Fig. 2D. Solid black curves are projections of the L=1 WT curve onto these planes, which also represents the standard-sized mutant embryos *tor*$^-$/*bcd*$^-$/*nos*$^-$, respectively. The predicted gap gene expression in these mutants can be read out along these lines (arrowheads on them are pointing from head to tail).

(D) Fate map $\tilde{y}(y)$ predicted for WT and another 11 different mutants (black lines) and the comparison with experimental measurements (yellow squares, cited from published works, see main text for references). See SI-7 for discussion on the panels of *mhb*$^-$ and *vas*$^-$*exu*$^-$*bcd6X*.

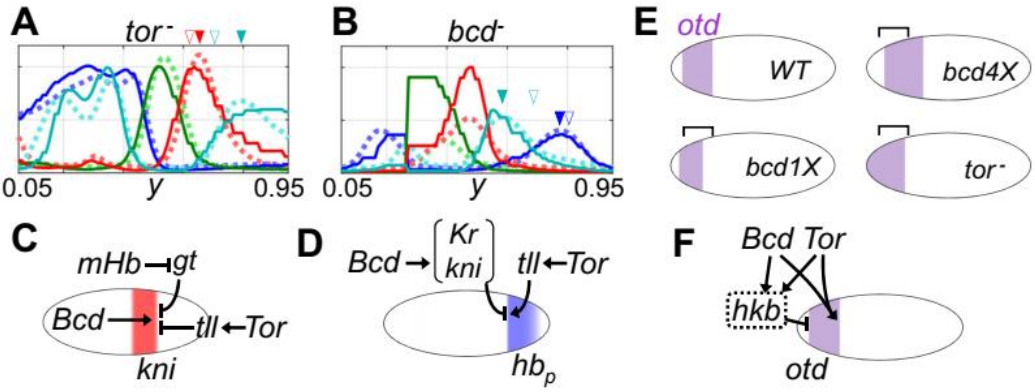

Figure 4. The decoder reveals information about regulation logic.

(A-B) The predicted gap gene patterns (solid lines) in *tor*$^-$ and *bcd*$^-$ are compared to that measured in (35) (dashed lines). The peak positions of the posterior *kni*, *hb* and *gt* domains are marked by filled arrowhead, their WT positions by the empty arrowheads.

(C) Redundant regulation on the posterior boundary of *kni* domain as required by scaling.

(D) According to the decoder, the vi-vii boundary ($\tilde{y}$=0.75) is set by the balance between the opposing gradients Bcd and Tor. Biochemically, this is realized by an indirect activation of Tor through *tll*, together with an indirect inhibition from Bcd, meditated by *Kr* and *kni*.

(E) The predicted expression patterns of the head gap gene *otd*, derived from the decoder. Structure of the decoder requires both Bcd and Tor to effectively activate *otd* for positioning its posterior boundary, while at the same time, both inhibit *otd* for defining its anterior boundary. This explains the *otd* regulations proposed by experimentalists decades ago (F). The decoding results on the bottom/left/back faces (marked by α/β/γ) of the cube in Fig. 2D. Solid black curves are projections of the L=1 WT curve onto these planes, which also represents the standard-sized mutant embryos *tor*$^-$/*bcd*$^-$/*nos*$^-$, respectively. The predicted gap gene expression in these mutants can be read out along these lines (arrowheads on them are pointing from head to tail).

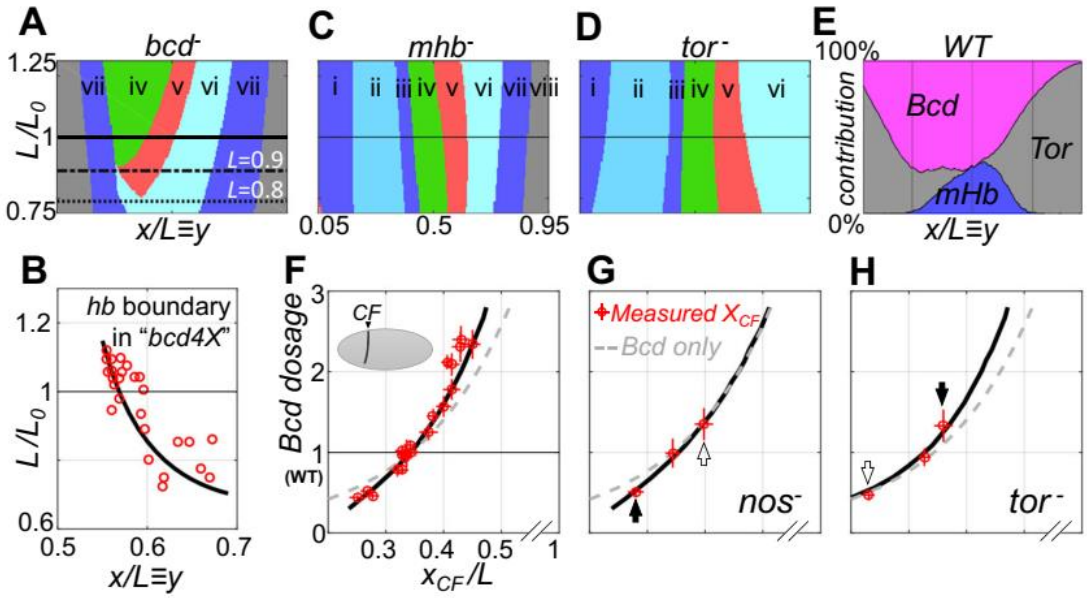

Figure 5. Different morphogens collaborate to achieve scaling in different regions.

(A) Missing Bcd destroys scaling throughout the embryo. In *bcd*$^-$, as L shrinks from 1.0 to 0.9 to 0.8 (solid, dashed and dotted lines), the *Kr* (iv) and *kni* (v) domains should disappear successively.

(B) The effect of Bcd dosage doubling on scaling is accurately captured by the decoder. The position of predicted (black line) vs. measured (red circles) (28) *hb* boundary (iii-iv boundary, $\tilde{y}$=0.47) are shown.

(C-D) In *mhb*$^-$ and *tor*$^-$, scaling is affected mostly in the middle and the two termini, respectively.

(E) Relative contributions of the three morphogens to scaling across the embryo.

(F) Shift of cephalic furrow (CF) under Bcd dosage change. Solid line is our prediction and red dots with error bars are from experiment data (40). Dashed grey line shows the position of the same Bcd concentration as CF in WT.

(G-H) Shift of CF position in *nos*$^-$ and *nos*$^-$ backgrounds, respectively.

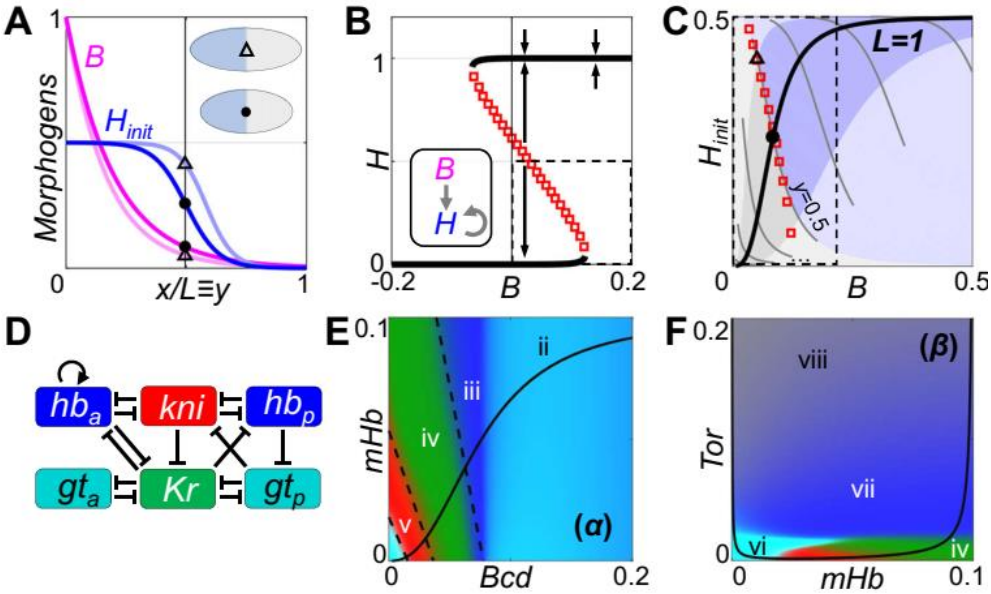

Figure 6. The scaling decoder can be implemented by gene regulation network.

(A) The profiles of two morphogens in a toy model, shown for two embryos of standard size (darker lines) and larger size (lighter lines).

(B) The bifurcation diagram for the network in the inset. A cell can reach one of the two bi-stable states depending on the values of the two morphogens, separated by the unstable manifold (red squares). This unstable manifold is the decision boundary separating the Hb-high and Hb-low fates. Its slope can be tuned by the activation strengths.

(C) Within the realistic L range (±20%, highlighted region), The y=0.5 line is well approximated by the decision boundary in (B) (red squares).

(D) The known gap gene network from Ref.*(33)*.

(E-F) The same plots as Fig. 3A-B, but using an ODE model of (D) (see SI-11 for details).